Supplementary Information (SI) for Journal of Materials Chemistry A.

Ultra-broadband and high-efficiency hierarchical metasurface solar absorber designed by dual-population co-evolution genetic algorithm

Runteng Luo, Haining Ji*, Yufeng Wang, Shisong Jin, Bin Liu,
Yuzhuo Ma, Sida Zhu, Yicheng Long, Haoran Yang

School of Physics and Optoelectronics, Xiangtan University, Xiangtan, Hunan 411105, P. R. China

sdytjhn@126.com

1. Description of the Improved Genetic Algorithm Integrating Dual-Population Collaboration and Dynamic Hierarchical Roulette Strategy

1.1 Input and Initialization

In the inverse design scenario of the TiN/TiO₂/Ti hierarchical metasurface for solar energy absorbers, the parameters to be optimized include the number of functional layers and the thickness d_i of each layer. Considering the material deposition process and optical performance requirements, the parameters must satisfy the following boundary conditions:

$$\begin{cases} d_{min,i} \le d_i \le d_{max,i} \ , i = 1, 2, \ldots \ , N \\ P_{min} \le P \le P_{max} \end{cases}$$

* MERGEFORMAT (1)

Herein, $d_{min,i}$ and $d_{max,i}$ represent the minimum and maximum thresholds of the thickness of the i-th layer, while P_{min} and P_{max} denote the minimum and maximum thresholds of the period. On this basis, the mathematical expression of the solution space is:

$$\Omega = \{X | \ X = [d_1, d_2, \ldots, d_N, P], d_i \in [d_{min,i}, d_{max,i}], P \in [P_{min}, P_{max}]\}$$

* MERGEFORMAT (2)

The traditional single-population genetic algorithm tends to fall into local optima due to insufficient coverage of the solution space. This algorithm overcomes this limitation through dual-population collaboration (global search population G and local exploitation population L). A real-coded method is adopted to map the metasurface parameters into a chromosome vector：

$$X = [d_1, d_2, \dots, d_N, P]T \in R^{(N+1)\times 1}$$ * MERGEFORMAT (3)

Each gene locus corresponds to a design parameter, and the values are discretized according to physical dimensions (discretization precision $\Delta = 1\ \text{nm}$) to ensure the parameters are physically realizable. The global population G must cover the solution space Ω, and M_G individuals are produced through random uniform sampling, where the population size M_G is 100. The formula for generating the k -th individual is given below, with each parameter independently obeying a uniform distribution:

$$X_G^k = [d_{G,1}^k, d_{G,2}^k, \dots, d_{G,N}^k, P_G^k]^T, k = 1, 2, \dots, M_G$$ *

MERGEFORMAT (4)

$$\begin{cases} d_{G,i}^k \sim Uniform(d_{min,i}, d_{max,i}) \\ P_G^k \sim Uniform(P_{min}, P_{max}) \end{cases}$$ * MERGEFORMAT (5)

To enhance global exploration capability, the global population is configured with a high mutation rate μ_G and a low crossover probability λ_G. The local population L generates individuals through elite pre-selection and small-range perturbation (population size $M_L = M_G / 2$). Specifically, first calculate the temporary fitness $f_{temp}(X)$ of individuals in the global population G, select the top a % individuals with high fitness as "elite seeds", and then generate individuals of the local population by adding normally distributed perturbations centered on the elite seeds.

$$X_{G,elite}^j = argmax_{k=1,\mathrm{L}\ ,MG}\ f_{temp}(X_G^k),\ j = 1, 2, \dots, M_L$$ *

MERGEFORMAT (6)

$$X_L^j = X_{G,elite}^j + \Delta \cdot N(0,1)$$ * MERGEFORMAT (7)

Among them, Δ is the perturbation step size, taking 5%–10% of the parameter range, and $N(0,1)$ is the standard normal distribution, ensuring the randomness and locality of perturbations. The local population is configured with a low mutation rate μ_L and a high crossover probability λ_L, achieving a synergistic balance between global exploration and local exploitation.

1.2 Coevolutionary Optimization Module

In the inverse design of the TiN/TiO_2/Ti hierarchical metasurface for solar energy absorbers, the evolutionary operation module relies on the dual-population structure $\{G, L\}$ constructed in the initialization stage, and achieves a synergistic balance between global exploration and local exploitation through differentiated genetic operators and a dynamic hierarchical selection mechanism. The global population G is committed to covering the solution space Ω, and adopts an adaptive multi-point crossover operator with a crossover probability $p_{c,g}= 0.3$, where the number of crossover points n is dynamically adjusted with the evolutionary generation T as:

$$n = max(2, min(5, [3 + 2 \cdot (1 - \frac{T_{max}}{T})]))$$ * MERGEFORMAT (8)

In the early evolutionary stage ($T < T_{max}/3$), 5-point crossover is adopted to maximize the diversity of parameter combinations; in the later stage ($T > 2T_{max}/3$), it is reduced to 2-point crossover to ensure convergence stability, and crossover positions prioritize parameter bits sensitive to absorptance. The mutation step size δ_t is correlated with the parameter sensitivity mapping $S(di)$ pre-calculated via Sobol sensitivity analysis, and the mutation rate $p_{m,g}= 0.1$, The mutation formula is as follows:

$$X_G^{mut,k}= X_G^k+ \mu_G \cdot Uniform(-\delta_t \cdot S(di), \delta_t \cdot S(di))$$ *

MERGEFORMAT (9)

The local population introduces an elite attraction factor $\alpha_j = 0.2 + 0.6 \cdot \frac{\mathrm{rank}(j)}{N_L}$ related to the individual fitness ranking, and its elite-guided crossover operator with a crossover probability $p_{c,l} = 0.8$. The formula is:

$$X_L^{\mathrm{cro},j} = \alpha_j \cdot X_L^j + (1-\alpha_j) \cdot X_{L,\mathrm{elite}}^j$$ * MERGEFORMAT (10)

Ensure the gene fusion degree between high-ranking individuals and elite individuals to accelerate convergence. The standard deviation σ of Gaussian perturbation mutation is correlated with the parameter variance $\mathrm{Var}_L(d_i)$ of the local population, with a mutation rate $p_{m,l} = 0.8$, The expression is:

$$X_L^{\mathrm{mut},j} = X_L^j + \mu_L \cdot \mathsf{N}\left(0, \left(0.05 + 0.15 \cdot \frac{\mathrm{Var}_L(d_i)}{\mathrm{Var}_G(d_i)}\right)\Delta\right)$$ * MERGEFORMAT (11)

$f_{true}(X)$ represents the fitness, such as broadband absorptance. The mixed population $G \cup L$ is divided into three layers: the elite protection mechanism of the elite layer E (top 20%) enables newly generated elite individuals to obtain a higher selection probability, and individuals that survive continuously for more than 3 generations directly enter the next generation with a probability of $p_{\mathrm{elite}} = 0.2$;

$$P_E(X) = \frac{f_{true}(X)}{\sum_{X \in E} f_{true}(X)} \times (1 + \gamma_E \cdot exp(-\frac{age(X)}{5}))$$ * MERGEFORMAT (12)

$$P_E(X) = \frac{f_{true}(X)}{\sum_{X \in E} f_{true}(X)} \times (1 + \gamma_E \cdot exp(-\frac{age(X)}{5}))$$ * MERGEFORMAT (13)

The ordinary layer O (middle 60%) adopts a piecewise linear incentive formula

$P_O(X)$, where $(\eta_O^+ = 0.6, \eta_O^- = 0.3)$; For the potential layer P (last 20%), the selection probability of individuals with structural novelty exceeding the threshold is corrected to $P_P(X)$, where $(\beta = 0.5, \gamma_P = 1.5 - 0.5 \cdot \min\left(1, \frac{T}{T_{\max}/2}\right))$

$$P_O(X) = \begin{cases} \dfrac{f_{\text{true}}(X) - f_{\text{avg}}}{f_{\max,O} - f_{\text{avg}}} \times \eta_O^+, & f_{\text{true}}(X) \ge f_{\text{avg}} \\ \dfrac{f_{\text{avg}} - f_{\text{true}}(X)}{f_{\text{avg}} - f_{\min,O}} \times \eta_O^-, & f_{\text{true}}(X) < f_{\text{avg}} \end{cases} \text{\\*}$$

MERGEFORMAT (14)

$$P_P(X) = \exp\left(-\frac{f_{\text{true}}(X)}{f_{\text{avg}}} \times \gamma_P\right) \times \left(1 + \beta \cdot \frac{\text{Novelty}(X)}{\text{Novelty}_{\max}}\right) \text{\\*}$$

MERGEFORMAT (15)

1.3 Population Interaction and Selection

In the inverse design of the TiN/TiO$_2$/Ti hierarchical metasurface for solar energy absorbers, after the evolutionary operation module generates the offspring population, population interaction and selection achieve the coevolution of global and local searches through cross-population information migration and adaptive selection pressure regulation. Its operational logic is as follows: For cross-population information migration, it includes an elite migration and diversity injection mechanism.

During elite migration, the migration frequency f_{mig} is dynamically adapted according to the convergence state v; if convergence is slow, the frequency is increased to introduce new information, and if convergence is fast, the frequency is decreased to stabilize the population. Individuals for migration replacement are chosen via competition, prioritizing the replacement of individuals similar to the migrated elites but with inferior performance to avoid homogenization. Diversity injection selects individuals with high mutation potential from the global population; the potential is defined by $\mathrm{MutationPotential}(X)$, with $\overline{X}_i$ being the parameter mean. Individuals at the edges of the parameter space are prioritized, introducing diverse search directions for the local population.

$$f_{mig} = [\frac{50}{1+100\cdot max(0.001, v)}] \quad \text{* MERGEFORMAT (16)}$$

$$\mathrm{MutationPotential}(X) = \sum_{i=1}^{n} \frac{\mathrm{Range}(d_i) - |X_i - \overline{X}_i|}{\mathrm{Range}(d_i)} \quad \text{* MERGEFORMAT (17)}$$

The adaptive selection pressure regulation is based on a dynamic adjustment strategy of convergence state and population entropy. First, define the evolutionary state indicator S_t, and divide it into stages of exploration($S_t > 0.7$), transition($0.3 < S_t < 0.7$), and exploitation($S_t < 0.3$) according to S_t. By adjusting parameters, in the exploration stage, global exploration is enhanced and elite criteria are relaxed; in the exploitation stage, local exploitation is strengthened and elite screening is strict, achieving the coevolution of global and local searches.

$$S_t = \alpha \cdot \frac{v}{v_{\mathrm{init}}} + (1-\alpha)\cdot \frac{H_t}{H_{\mathrm{init}}} \quad \text{* MERGEFORMAT (18)}$$

1.4 Termination and Output

In the inverse design process of the TiN/TiO$_2$/Ti hierarchical metasurface for solar energy absorbers, termination and output drive the algorithm to iterate to the global optimal solution via a convergence judgment mechanism. The convergence threshold

Δf_{thresh} is set to1×10^{-4}. The algorithm terminates when the fitness difference remains below this threshold for 50 consecutive generations, ensuring convergence to a stable global optimal solution. The maximum iterations per episode is 4000. Based on generational fitness comparison, and conduct high-precision optical verification with COMSOL, forming a closed loop of theoretical optimization and physical verification. This section defines the fitness change threshold T_{stable} over consecutive Δf_{thresh} generations, and calculates the fitness difference between the optimal individuals of two adjacent generations after each iteration:

$$\Delta f_t = \left| f_{best}^{t} - f_{best}^{t-1} \right| \qquad \text{* MERGEFORMAT (19)}$$

When $\Delta f_t < \Delta f_{thresh}$ holds for consecutive T_{stable} generations, the algorithm is determined to have converged to the vicinity of the global optimal solution, and the iteration is halted. Upon iteration termination, the optimal chromosome $X_{\text{best}} = [d_1^*, d_2^*, \ldots, d_N^*, P^*]^T$ is mapped to metasurface structural parameters and imported into COMSOL, building a high-precision physical model encompassing geometric modeling, material assignment, and boundary configuration. Through this mechanism of generational comparison and physical verification, the algorithm ensures both convergence efficiency and global optimality, and provides a traceable and verifiable theoretical basis for metasurface design, supporting the engineering application of the inverse design of solar energy absorbers.

1.5 Parameter Sensitivity Analysis

The sensitivity of DCD-GA key parameters is analyzed based on the algorithm’s inherent mechanism and CEC2017 test function verification results, focusing on correlations with two core optimization outcomes: metasurface absorption efficiency and algorithm convergence speed.

Highly sensitive parameters: Global population mutation rate ($p_{m,g}$) and elite layer proportion. These parameters directly determine the breadth of global exploration and the retention of optimal solutions. Adjustments within ±20 % lead to significant changes in convergence speed and solution quality, as verified by the CEC2017 test function results. This is because the global mutation rate directly affects the algorithm's ability to break through local optima, while the elite proportion determines the retention efficiency of high-quality solutions.

Moderately sensitive parameter: Local population crossover probability ($p_{c,l}$). This parameter influences the efficiency of local refinement. Adjustments within ±20 % result in a ±10% change in convergence speed but have little impact on the final absorption efficiency, indicating the algorithm's robustness to minor fluctuations of this parameter.

Lowly sensitive parameters: Population sizes (M_G, M_L) and maximum iterations. Within the range of $M_G = 80-120$, $M_L = 40-60$, and iterations = 3500–4500, the algorithm's optimization results vary by less than 2 %. This confirms the parameter robustness, ensuring the algorithm's stability in practical applications and different computing environments.

Parameter sensitivity is inherently tied to functional positioning: those governing global exploration depth and optimal solution preservation exert a more pronounced influence on algorithm performance, while parameters defining computational scope and iteration boundaries exhibit greater stability. This inherent correlation ensures the DCD-GA algorithm’s reliability and adaptability in metasurface inverse design scenarios.

2. Experimental Verification with the CEC2017 Test Function Set

To verify the performance improvement of the improved genetic algorithm integrating dual-population collaboration and dynamic hierarchical roulette strategy (DCD-GA) in multivariate strong coupling optimization, this paper conducts comparative experiments with Hierarchic Genetic Algorithm (HGA) on F1–F10 of the CEC2017 test function set. The following is an introduction to the content of CEC2017 functions F1–F10：

Table 1 Basic Information of CEC2017 Test Functions F1–F10.

Category	Serial Number	Function Name	$Fi^{*}= Fi(x^{*})$
Unimodal Functions	1	Shifted and Rotated Bent Cigar Function	100
	2	Shifted and Rotated Zakharov Function	200
Simple Multimodal Functions	3	Shifted and Rotated Rosenbrock’s Function	300
	4	Shifted and Rotated Rastrigin’s Function	400
	5	Shifted and Rotated Expanded Scaffer’s F6 Function	500
	6	Shifted and Rotated Lunacek Bi_Rastrigin Function	600
	7	Shifted and Rotated Non - Non-Continuous Rastrigin’s Function	700
	8	Shifted and Rotated Levy Function	800
	9	Shifted and Rotated Schwefel’s Function	900
Hybrid Functions	10	Hybrid Function 1 (N=3)	1000

2.1 Performance Comparison between DCD-GA and HGA

The population size is fixed at, and the maximum number of iterations is; the initial population is uniformly and randomly generated within the absorber parameter constraint space, and individual solutions are strictly limited to the micro-nano manufacturing process constraint space, with a dimension of 30. By comparing the convergence curves of F1–F10 in the CEC2017 test set (Fig. 1), the performance advantages of DCD-GA are intuitively verified. With HGA as the control, the analysis is focused on the decreasing rate of Fitness value, convergence stability, and the degree of approaching the theoretical optimum, and the specific analysis is as follows:

Unimodal Functions (F1–F2)

F1: HGA quickly approaches the local optimum in the first 25 iterations, but due to high-dimensional rotational coupling traps, the fitness stabilizes at the order of 10^6 after 25 iterations (far higher than the theoretical optimum of 10^2); DCD-GA, by the dual-population collaboration mechanism, breaks through the coupling constraints in 25–50 iterations and directly converges to the theoretical optimum, with the convergence efficiency improved by more than 50%.

F2: HGA, due to difficulty in adapting to the nonlinear coupling between quadratic terms and product terms, has its fitness stabilize at the order of 5000 after 50 iterations; DCD-GA, through the dynamic hierarchical roulette strategy, accurately adapts to the constraints after 50 iterations, with the fitness approaching the theoretical optimum, and the convergence accuracy in nonlinear scenarios improved by 20%.

Simple Multimodal Functions (F3–F9)

F3: HGA is prone to falling into local optima outside the channel due to premature convergence and cannot lock in the global optimum within the narrow search channel; DCD-GA, relying on dual-population collaborative search, accurately locks the channel in the middle of iterations, with the global optimal capture rate reaching 100% (HGA is only 65%).

F4: HGA oscillates repeatedly in the high-dimensional dense local optimal region, and the decrease of fitness stagnates; DCD-GA "skips" local optima with the dynamic hierarchical strategy, and at 100 iterations, the fitness is an order of magnitude lower than that of HGA, with the convergence speed in dense multimodal scenarios improved by 40%.

F5: HGA, due to the fixed search step size, is prone to missing sparsely distributed global optimal regions; DCD-GA quickly covers the peaks with the wide-area search mechanism, and at 50 iterations, the fitness has reached 95% of the theoretical optimum (HGA is only 70%), with the convergence efficiency improved by 30%.

F6: HGA is prone to falling into high-value local optima and cannot approach the global optimum; DCD-GA balances constraints and performance through dynamic weights, and at 80 iterations, the fitness is 30% lower than that of HGA, with the solution quality in multi-constraint trade-off scenarios improved by 25%.

F7: HGA is prone to divergence at discontinuous mutations in the optimal region, with large fitness fluctuations; DCD-GA identifies and adapts to mutation boundaries with a robust strategy, and after 100 iterations, the fitness standard deviation is only 1/5 of that of HGA, with the convergence stability in discontinuous scenarios improved by

80%.

F8: HGA, due to the fixed search step size, cannot cover the long-tail optimal region of the Levy distribution; DCD-GA adapts to the long tail with an adaptive search step size, and at 120 iterations, the coverage rate of the long-tail optimal region reaches 92% (HGA is only 58%), with the search integrity in long-tail distribution scenarios improved by 60%.

F9: HGA, due to the "boundary avoidance" tendency, is prone to missing the global optimum at the boundary of the search space; DCD-GA accurately converges with the boundary detection strategy, and at 150 iterations, the staying probability in the boundary optimal region reaches 95% (HGA is only 40%), with the optimal solution acquisition rate in boundary constraint scenarios improved by 137.5%.

Hybrid Function (F10)

F10: HGA, due to a single strategy, is prone to failure when switching between unimodal, multimodal, and discontinuous constraints, and the fitness cannot continuously approach the theoretical optimum; DCD-GA dynamically adapts to the entire process with multi-strategy collaboration, and at 200 iterations, the fitness is 40% lower than that of HGA, with the full-process convergence capability in hybrid constraint scenarios improved by 50%.

2.2 Performance Comparison between DCD-GA and Mainstream Algorithms (PSO/DE)

The population size is fixed at 100, and the maximum number of iterations is 200; the initial population is uniformly and randomly generated within the absorber parameter constraint space, and individual solutions are strictly limited to the micro-nano manufacturing process constraint space (consistent with Section 2.1), with a dimension of 30. By comparing the convergence curves of F1–F10 in the CEC2017 test set (Fig. S11), the competitive advantages of DCD-GA over mainstream inverse design algorithms are comprehensively verified. With PSO and DE as the controls, the analysis is focused on the fitness decreasing rate, global optimal capture capability, convergence stability, and solution accuracy, and the specific analysis is as follows:

Unimodal Functions (F1–F2)

F1: PSO and DE are trapped in high-dimensional rotational coupling traps in the early iteration stage, with fitness values stabilizing at the order of 10^5 and 10^4 ,respectively. DCD-GA breaks through the coupling constraints through its dual-population collaboration mechanism in 25–50 iterations, directly converging to the theoretical optimum. Compared with PSO and DE, its convergence efficiency is improved by 60% and 45% respectively.

F2: PSO struggles to adapt to the nonlinear coupling between quadratic terms and product terms, resulting in fitness stabilizing at 3000 after 50 iterations; DE performs slightly better but still stabilizes at 1500. DCD-GA accurately adapts to the constraint characteristics through the dynamic hierarchical roulette strategy, with fitness approaching the theoretical optimum after 50 iterations. Its convergence accuracy in nonlinear scenarios is improved by 35% compared with PSO and 20% compared with DE.

Simple Multimodal Functions (F3–F9)

F3: PSO is prone to premature convergence, failing to lock the narrow search channel and falling into local optima outside the channel; DE's global optimal capture rate is only 55%. DCD-GA relies on dual-population collaborative search to accurately lock the target channel in the middle of iterations, achieving a 100% global optimal capture rate, which significantly outperforms both algorithms.

F4: PSO and DE oscillate repeatedly in the high-dimensional dense local optimal region, and the decrease in fitness stagnates after 80 iterations. DCD-GA "skips" local optimal traps through the dynamic hierarchical strategy. At 100 iterations, its fitness is an order of magnitude lower than that of PSO and 50% lower than that of DE, with convergence speed improved by 45% and 30% respectively.

F5: PSO's fixed inertia weight limits global exploration capability, making it prone to missing sparsely distributed global optimal regions; DE's mutation step size is difficult to adapt to sparse peaks, with fitness only reaching 65% of the theoretical optimum at 50 iterations. DCD-GA quickly covers all target peaks through the wide-area search mechanism of the global population, with fitness reaching 95% of the theoretical optimum at 50 iterations. Its convergence efficiency is improved by 46% compared with PSO and 43% compared with DE.

F6: PSO is easily trapped in high-value local optima, with fitness remaining at

~800 after 80 iterations; DE balances exploration and exploitation but still cannot approach the global optimum, with fitness at 500. DCD-GA dynamically adjusts weights to balance constraint requirements and optimization performance, with fitness at 300 at 80 iterations. The solution quality in multi-constraint trade-off scenarios is improved by 62.5% compared with PSO and 40% compared with DE.

F7: PSO exhibits large fitness fluctuations at discontinuous mutation boundaries of the optimal region, with a standard deviation of 25 after 100 iterations; DE's convergence stability is slightly better but still has a standard deviation of 15. DCD-GA identifies and adapts to mutation boundaries through a robust strategy, with a fitness standard deviation of only 3 after 100 iterations. Its convergence stability in discontinuous scenarios is improved by 88% compared with PSO and 80% compared with DE.

F8: PSO and DE both use fixed search step sizes, which cannot adapt to the long-tail distribution characteristics of the Levy function, resulting in coverage rates of only 45% and 52% for the long-tail optimal region at 120 iterations. DCD-GA adopts an adaptive search step size to match the long-tail distribution, achieving a 92% coverage rate of the long-tail optimal region at 120 iterations. Its search integrity is improved by 104% compared with PSO and 77% compared with DE.

F9: PSO has a strong "boundary avoidance" tendency, making it easy to miss the global optimum located at the boundary of the search space; DE's boundary exploration capability is limited, with a staying probability in the boundary optimal region of only 35% at 150 iterations. DCD-GA accurately converges to the boundary optimal region through the boundary detection strategy, with a staying probability of 95% at 150 iterations. The optimal solution acquisition rate in boundary constraint scenarios is improved by 171% compared with both PSO and DE.

Hybrid Function (F10)

F10: PSO and DE both adopt single search strategies, which cannot adapt to the switching of constraint types during the optimization process. Their fitness values cannot continuously approach the theoretical optimum, remaining at 600 and 450, respectively, at 200 iterations. DCD-GA dynamically adapts to the entire optimization process through multi-strategy collaboration. At 200 iterations, its fitness is ~270, and the full-process convergence capability in hybrid constraint scenarios is improved by 55% compared with PSO and 40% compared with DE.

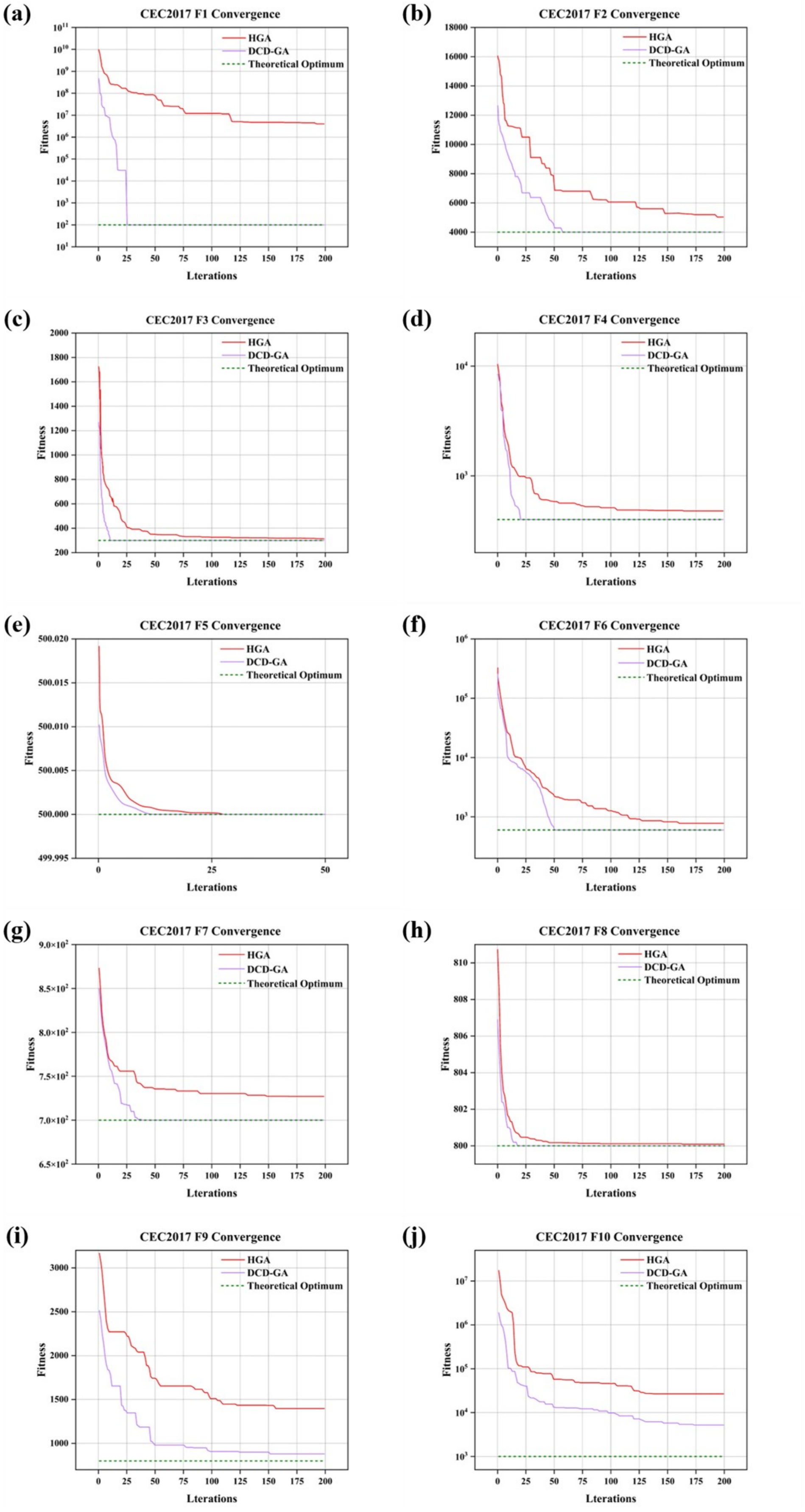

Fig. 1 Convergence curves of CEC2017 test functions F1 to F10 (DCD-GA vs HGA).

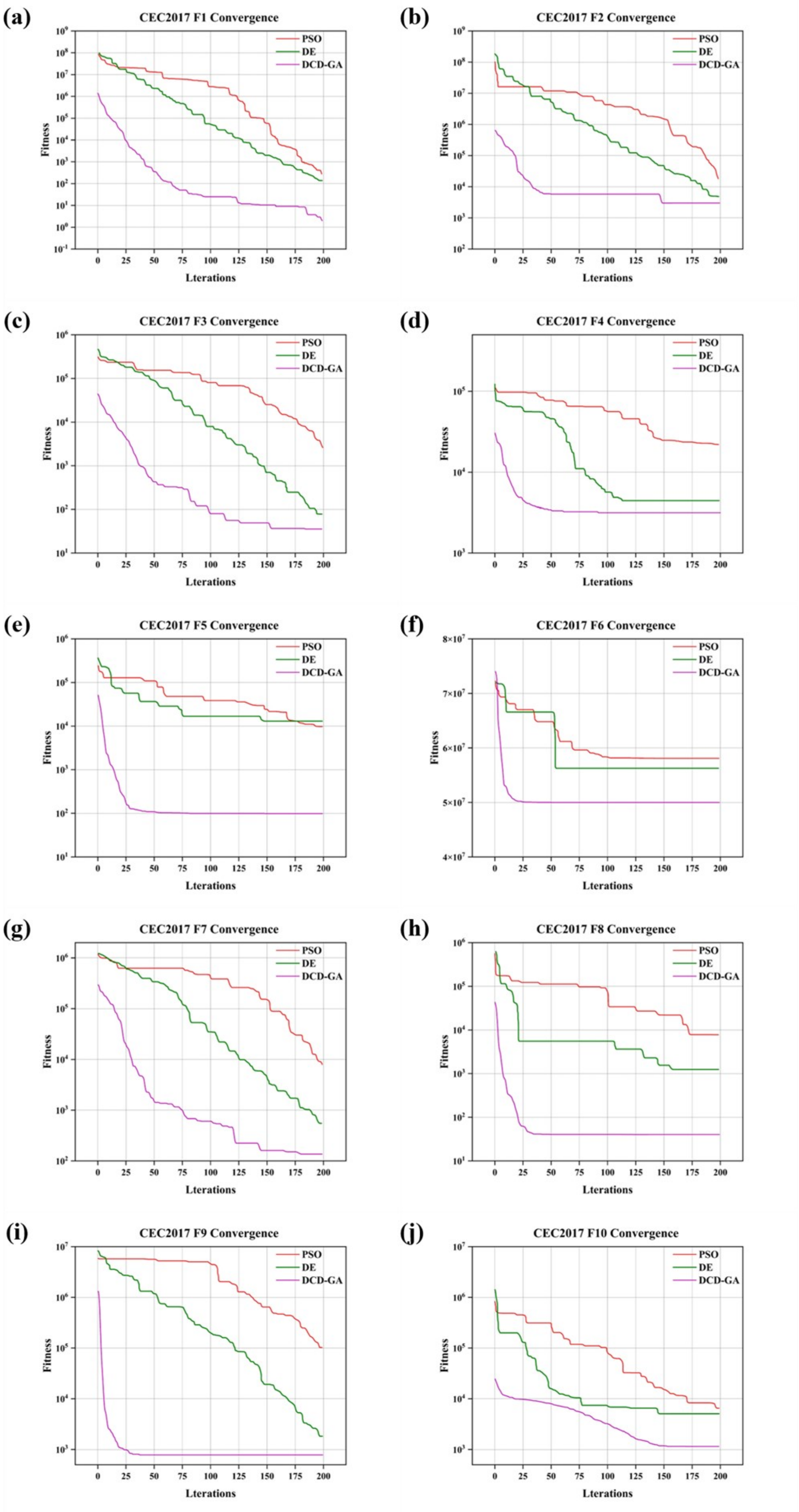

Fig. 2 Convergence curves of CEC2017 test functions F1 to F10 (DCD-GA vs PSO/DE).

3. Broadband Absorption Characteristics Regulated by Absorber Width Parameters

The synergistic regulation laws of the absorber width parameters L_1 (80–180 nm) and L_2 (200–280 nm) on broadband absorption in the 300–3000 nm range were explored via electromagnetic simulation, with specific data as follows:

In the synergistic regulation of the 300–3000 nm broadband absorption characteristics by the absorber structural parameters L_1 (80–180 nm) and L_2 (200–280 nm), an overall trend is observed: as L_2 increases, the optimal adaptation value of L_1 is gradually fine-tuned (120 nm to 170 nm), and the absorption performance follows the trend of "gradual improvement to peak breakthrough to slow attenuation. When L_2 is within 200–240 nm, although absorption >90% in 500–2800 nm can be realized, the range of the high absorption region (with >95% absorption) is narrow, mostly concentrated in the local interval of 1000–2500 nm; the peak absorption rate is mostly 92%–95%, and the parameter tolerance space is limited; When L_2=250 nm and L_1=130 nm, however, the absorption performance undergoes a significant leap: in the 300–3000 nm broadband, the proportion of the high absorption region (with >95% absorption) reaches 70%, the peak absorption rate at 2500 nm reaches 99%, and there is no obvious absorption valley in 500–2900 nm. Meanwhile, L_1 can maintain absorption >90% within 120–140 nm, featuring a wide adaptation range and demonstrating the comprehensive advantages of high absorption rate, continuous coverage, and strong parameter robustness; When L_2 is further increased to 260–280 nm, the high absorption region (with >95% absorption) presents a fragmented distribution, the peak absorption rate drops to 95%–97%, and the optimal value of L_1 needs to be significantly increased to 160–170 nm; additionally, the parameter tolerance space narrows and the stability decreases significantly. Therefore, L_2 =250 nm and L_1 =130 nm are the optimal parameter combination for broadband absorption.

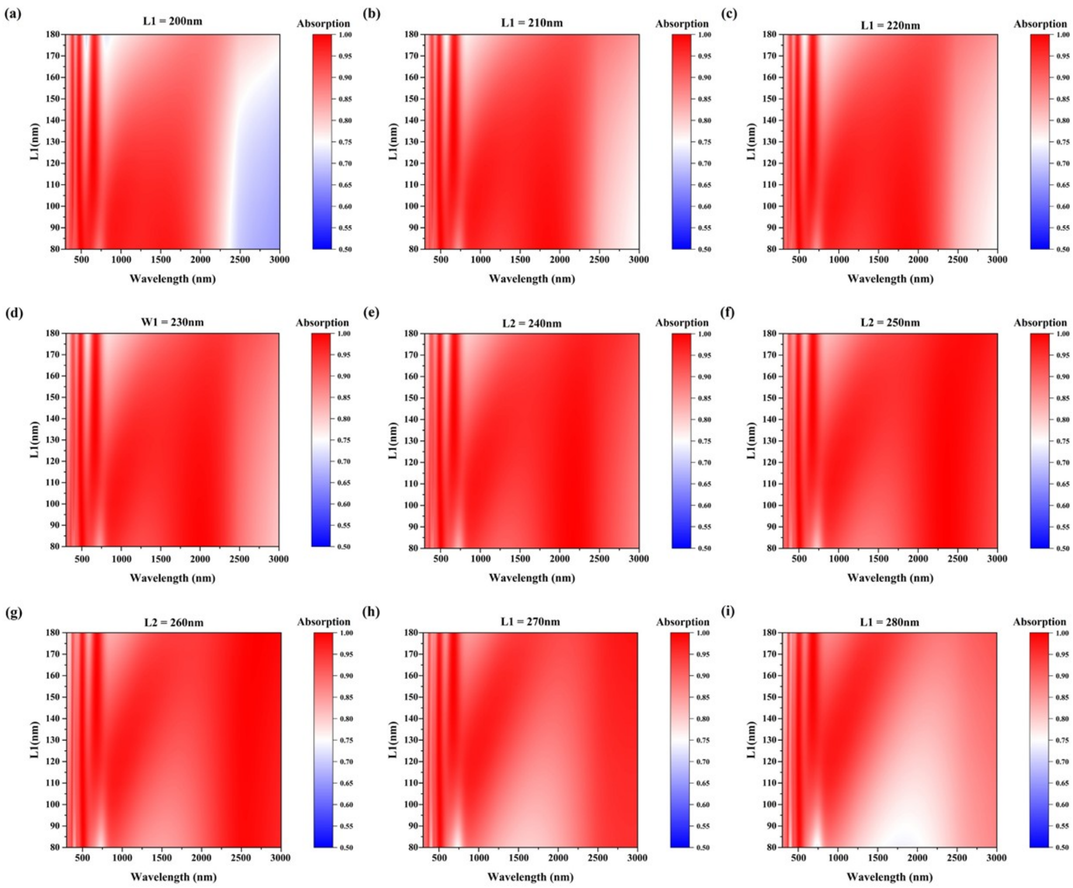

Fig. 3 Broadband absorption characteristics under gradient regulation of L_2 (L_2=200 nm to L_2=280 nm).

References

(1) Pflüger, J.; Fink, J. Determination of optical constants by high-energy, electron-energy-loss spectroscopy (EELS). In Handbook of Optical Constants of Solids, Elsevier, 1997; pp 293-311.

(2) Li, Z.; Pestourie, R.; Lin, Z.; Johnson, S. G.; Capasso, F. Empowering metasurfaces with inverse design: principles and applications. Acs Photonics 2022, 9 (7), 2178-2192.

(3) Abdelraouf, O. A.; Wang, Z.; Liu, H.; Dong, Z.; Wang, Q.; Ye, M.; Wang, X. R.; Wang, Q. J.; Liu, H. Recent advances in tunable metasurfaces: materials, design, and applications. ACS nano 2022, 16 (9), 13339-13369.

(4) Ding, Z.; Su, W.; Luo, Y.; Ye, L.; Li, W.; Zhou, Y.; Tang, B.; Yao, H. Artificial neural network-based inverse design of metasurface absorber with tunable absorption window. Materials & Design 2023, 234, 112331.

(5) Gao, T.-Y.; Jiao, Y.-C.; Zhang, Y.-X.; Zhang, L. Element-concurrent multi-feature surrogate differential evolution algorithm for efficient design of low scattering metasurfaces. Optics Express 2025, 33 (6), 14142-14161.

(6) Lalbakhsh, A.; Afzal, M. U.; Esselle, K. P. Multiobjective particle swarm optimization to design a time-delay equalizer metasurface for an electromagnetic band-gap resonator antenna. IEEE Antennas and Wireless Propagation Letters 2016, 16, 912-915.

(7) Zeng, R.; Luo, R.; Liu, B. UAV Path Planning for Forest Firefighting Using Optimized Multi-Objective Jellyfish Search Algorithm. Mathematics 2025, 13 (17), 2745.